RSC Advances

PAPER

View Article Online
View Journal | View Issue

Cite this: *RSC Adv.*, 2025, **15**, 41479

Combined DFT and experimental study of CuO and Ni–CuO nanoparticles: structural characterization, photocatalytic degradation, and antimicrobial activities

Syeda Shakila Akter, *[a] Md. Hasinul Babu, [a] Sake Millat Imame, [b] M. Kamrul Hossain *[a] and Faisal I. Chowdhury *[a]

In this study, pure and nickel-doped copper oxide (CuO and Ni–CuO) nanoparticles were synthesized *via* a sol–gel route and comprehensively characterized to investigate their structural, electronic, photocatalytic, and antimicrobial properties. X-ray diffraction (XRD) confirmed the formation of monoclinic CuO with successful Ni incorporation, evidenced by peak broadening and lattice strain. Field emission scanning electron microscopy (FESEM) and energy-dispersive X-ray spectroscopy (EDX) analyses revealed quasi-spherical morphologies and homogeneous Ni doping, while FTIR spectra confirmed Cu–O bonding with subtle changes induced by Ni substitution. Photocatalytic degradation of methylene violet (MV) dye under UV irradiation demonstrated enhanced efficiency for Ni–CuO (88.62% at 20 ppm) compared to pure CuO (84.92%), with kinetics following a pseudo-first-order model. Additionally, Ni–CuO exhibited improved antimicrobial activity against Gram-positive and Gram-negative bacteria as well as *Candida albicans*, achieving up to 99.72% inhibition at 250 μg mL^{-1}. To support the antimicrobial findings, molecular docking studies were performed using Cu_4O_4 and Ni-doped Cu_3NiO_4 nanoclusters against microbial target proteins. The Ni-doped nanocluster displayed stronger binding affinities with key proteins from *E. coli*, *S. typhi*, and *Candida albicans*, forming stabilizing interactions such as hydrogen bonds, metal–acceptor contacts, and π–sulfur bonds. These interactions were especially pronounced in the *Candida* model, aligning well with experimental inhibition data. Density Functional Theory (DFT) calculations on Cu_4O_4 and Ni-doped Cu_3NiO_4 nanoclusters revealed modifications in bond lengths, HOMO–LUMO gaps, and charge distribution upon doping, which correlated well with experimental observations. Notably, partial density of states (PDOS) and charge analyses indicated increased electronic delocalization and orbital hybridization in Ni–CuO, supporting its superior photocatalytic and antimicrobial performance. This integrative study provides atomistic insight into the structure–property relationships of doped CuO nanostructures, underscoring their potential for multifunctional environmental and biomedical applications.

Received 23rd August 2025
Accepted 19th October 2025

DOI: 10.1039/d5ra06284e

rsc.li/rsc-advances

1. Introduction

In recent years, the development of efficient, low-cost, and environmentally friendly nanomaterials has attracted significant attention for applications in environmental remediation and biomedical fields.[1] Among various transition metal oxides, copper oxide (CuO) has emerged as a promising candidate due to its narrow band gap (\~1.2 eV), high stability, abundance, and strong optical absorption in the visible region. CuO nanoparticles (NPs) exhibit considerable potential in photocatalysis, antimicrobial applications, gas sensing, lithium-ion batteries, and solar energy conversion. However, the practical performance of CuO-based systems is often limited by rapid electron–hole recombination, low surface reactivity, and structural instability under operational conditions.[2]

To overcome these limitations, doping CuO with foreign metal ions has been explored as an effective strategy to tailor its structural, optical, and electronic properties. Among the various dopants, nickel (Ni) is particularly attractive due to its similar ionic radius to Cu^{2+} and its ability to substitute into the CuO lattice without drastically disrupting the host crystal structure. Ni doping can modulate the electronic band structure, enhance charge separation, introduce defect states, and improve overall catalytic efficiency.[3] Moreover, transition metal doping may influence the antimicrobial properties of CuO by altering

[a]*Department of Chemistry, University of Chittagong, Chittagong-4331, Bangladesh. E-mail: kamrulch@cu.ac.bd; faisal@cu.ac.bd; syedashakilaakter.chem@std.cu.ac.bd*
[b]*Department of Applied Chemistry and Chemical Engineering, University of Chittagong, Chittagong-4331, Bangladesh*

surface charge distribution and enhancing reactive oxygen species (ROS) generation.[4]

Despite numerous studies on CuO-based nanostructures, a comprehensive understanding of the correlation between Ni doping, structural modification, electronic properties, and functional performance remains incomplete. In particular, limited reports exist that integrate experimental characterization with first-principles density functional theory (DFT) calculations to gain atomistic insights into the electronic structure and charge redistribution in Ni–CuO nanoclusters.[5]

In this work, we synthesized pure and Ni–CuO nanoparticles *via* a facile sol–gel method using citric acid as a chelating agent and CTAB as a stabilizer. The structural, morphological, and chemical properties of the synthesized samples were systematically characterized by X-ray diffraction (XRD), field emission scanning electron microscopy (FESEM), energy-dispersive X-ray spectroscopy (EDX), and Fourier-transform infrared (FTIR) spectroscopy. The photocatalytic activity was evaluated by degrading methylene violet (MV) dye under ultraviolet light, and antimicrobial efficacy was assessed against both Gram-positive and Gram-negative bacterial strains, as well as *Candida* species.

To complement the experimental findings, we performed spin-unrestricted DFT calculations using ORCA software to model the electronic structures of Cu_4O_4 and Cu_3NiO_4 nanoclusters.[5] Structural optimization, HOMO–LUMO analysis, charge distribution (*via* Hirshfeld, Mulliken, and Löwdin schemes), and projected density of states (PDOS) calculations were conducted to elucidate the influence of Ni doping at the atomic level. In addition, molecular docking studies were conducted against Gram-positive and Gram-negative bacterial strains, as well as *Candida* species to assess their possible interactions and inhibitory effects of the Cu_4O_4 and Ni-doped Cu_4O_4 (Cu_3NiO_4) nanoclusters. The selected targets included *Bacillus cereus* (PDB ID: 1BMC),[6] *Candida albicans* (PDB ID: 6AKZ),[7] *Escherichia coli* (PDB ID: 3ZMI),[8] *Salmonella typhi* (PDB ID: 6IAI),[9] and *Staphylococcus aureus* (PDB ID: 4QLO).[10] The integrated experimental-theoretical approach in this study provides new insights into the structure–property–performance relationships in Ni–CuO nanostructures and highlights their potential for multifunctional applications in environmental and biomedical domains.

2. Materials and methodology

2.1 Materials

All of the reagents used in this study were analytical grade and did not require any further purification. Merck (Germany) provided the following chemicals: cetyltrimethylammonium bromide (CTAB), citric acid monohydrate, ethanol, nickel(II) nitrate hexahydrate ($Ni(NO_3)_2 \cdot 6H_2O$), and copper(II) nitrate trihydrate ($Cu(NO_3)_2 \cdot 3H_2O$).[11–15] The entire synthesis procedure was carried out using deionized (DI) water.

2.2 Synthesis of CuO and Ni-doped CuO nanoparticles

CuO and Ni–CuO nanoparticles were synthesized utilizing a sol–gel technique using ethanol and deionized water as solvents.[12,13] After dissolving copper(II) nitrate trihydrate in the solvent mixture, citric acid was added as a chelating agent and the ratio was 1 : 1 (CN : CA).[15] A stabilizer called cetyltrimethylammonium bromide (CTAB) was used to stop agglomeration.[13,15] Sodium hydroxide (NaOH) was used to bring the pH down to about 7 while the mixture was constantly stirred at 50 to 60 degrees Celsius.[16] The Ni-doped sample was prepared by adding 2 mol% of nickel(II) nitrate hexahydrate to the precursor solution employing the same method of sol–gel synthesis as previously mentioned.[12] Once the gels had formed, they were dried and ground into fine powders. After that, these powders were calcined for four hours at 600 °C in an air environment in a muffle furnace to create the final nanoparticles.[17]

2.3 Characterization techniques

The structural, morphological, elemental, and chemical bonding properties of the synthesized CuO and Ni–CuO nanoparticles were examined using a combination of powder X-ray diffraction (XRD), scanning electron microscopy (SEM), energy-dispersive X-ray spectroscopy (EDX), and Fourier-transform infrared spectroscopy (FTIR) techniques.[11–14,16]

2.3.1 XRD analysis. A GBC EMMA X-ray diffractometer (Mini Material Analyzer) was used to do structural analysis. The Cu Kα radiation ($\lambda = 1.5406$ Å) produced by a copper target was used to record the diffraction patterns. The operating voltage and current were 40 kV and 40 mA, respectively, and the scan was conducted over a 2θ range of 10° to 90°. Data were digitally stored for post-processing, and the instrument was completely computer-controlled.

2.3.2 SEM and EDX analysis. An MA15 VP-SEM (Carl Zeiss EVO, UK) with spatial resolution between 50 and 100 nm and magnifications ranging from 20× to 30 000× was used to examine the surface morphology of the nanoparticles. The SEM study shed light on the distribution, aggregation, and morphology of the particles. A SEM-integrated energy-dispersive X-ray spectroscopy (EDX) instrument, which identifies elemental presence and distribution by detecting distinctive X-ray emissions from the sample, was used to establish the elemental composition.

2.3.3 FTIR analysis. The Shimadzu IR Affinity-1S spectrometer, which has a MIRacle 10 ATR attachment, was used to record Fourier-transform infrared (FTIR) spectra. At room temperature, the spectra were measured between 400 and 4000 cm^{-1}. Advanced dynamic alignment for increased stability and an airtight interferometer chamber with an automatic internal dehumidifier to reduce environmental impact during analysis are features of the system.

2.4 Photocatalytic activity test

The photocatalytic activity of the synthesized CuO and Ni–CuO nanoparticles were assessed using methylene violet (MV) dye at initial concentrations of 15 ppm and 20 ppm. A photocatalyst dosage of 500 mg L^{-1} was dispersed in 100 mL of dye solution and magnetically stirred at 600 rpm. The suspension was kept in the dark for 30 minutes to ensure adsorption–desorption equilibrium. Photocatalytic degradation was carried out under

ultraviolet (UV) irradiation using a 125 W mercury lamp positioned 10 cm above the sample surface. The reaction mixture was contained in borosilicate glass vessels. Absorbance measurements were taken at 580–592 nm (characteristic of MV) using a Shimadzu UV-1800 spectrophotometer and a silicon photodiode detector was employed to monitor light intensity. All experiments were conducted at ambient temperature, and degradation efficiency was calculated based on the decrease in dye absorbance over time.

2.5 Antimicrobial activity test

The antimicrobial activity of the synthesized CuO and Ni–CuO nanoparticles were evaluated using the agar well diffusion method, a standard method for the initial screening of antimicrobial agents.[18] To evaluate the broad-spectrum activity of the nanoparticles, five distinct microbial strains were selected: a fungal strain (*Candida albicans*), Gram-positive bacteria (*Bacillus cereus*, *Staphylococcus aureus*), and Gram-negative bacteria (*Escherichia coli*, *Salmonella typhi*).[19] A nutrient broth was used to cultivate each microbial strain, and the 0.5 McFarland standard (about 1.5×10^8 CFU mL^{-1}) was applied.[20] Mueller–Hinton Agar (MHA) plates were utilized for bacterial strains, while Sabouraud Dextrose Agar (SDA) was used to cultivate *Candida albicans*. Sterile cotton swabs were used to uniformly inoculate the prepared agar plates to ensure consistent lawn formation.[20] A cork borer was utilized to create sterile wells with a diameter of 6 mm in the agar surface, and 50 μL of CuO and 50 μL of Ni–CuO nanoparticle suspensions at concentrations of 50, 100, 150, 200, and 250 μg mL^{-1} were added to each well. All experiments were conducted under aseptic conditions with a negative control (solvent only) to verify the absence of inherent antibacterial activity. The zones of inhibition (ZOI) surrounding each well were measured in millimeters using a digital Vernier caliper following 24 hours of incubation at 37 °C.[18] All experiments were performed in triplicate, and the results were reported as the mean ± standard deviation. Based on diffusion characteristics and inhibitory patterns of the tested compounds, this method facilitates the qualitative and semi-quantitative evaluation of antimicrobial efficacy. Future research may use minimum bactericidal concentration (MBC) and minimum inhibitory concentration (MIC) assays to enable a more accurate and quantitative evaluation of antimicrobial potency, while the agar diffusion method provides useful preliminary insights.[18,21]

2.6 Computational method (DFT)

The experimental study was complemented by Density Functional Theory (DFT) calculations to provide atomistic insights understanding of the electronic and structural properties of the synthesized CuO and Cu_3NiO_4 nanoclusters. The ORCA 5.0.4 quantum chemistry software package was used for all calculations. In combination with the *def2-SVP* basis set, geometry optimizations were carried out using the BP86 generalized gradient approximation (GGA) functional, which offers a reliable balance between computational efficiency and accuracy for transition metal oxide systems.[22] Geometry optimizations were restricted to 200 iterations, and the *SlowConv* keyword and an increased SCF cycle limit of 800 iterations were used to guarantee convergence of open-shell configurations.[22] Cu_4O_4 and Cu_3NiO_4 clusters were employed as finite-sized models in these computations. The effects of doping spin states, and charge redistribution in transition metal oxides are frequently assessed using these models, which also provide meaningful correlation with experimental reactivity and electronic properties. Spin-state testing was performed for all clusters to determine their ground-state configurations. For pristine Cu_4O_4, the triplet state was found to be more stable than the singlet. For Cu_3NiO_4, the doublet state converged successfully over the quartet and was used in further calculations. The gas phase was used for all calculations in order to simulate isolated nanoclusters. Single-point energy calculations were conducted to extract electronic relevant descriptors and refine total energies following geometry optimization. The electronic stability and reactivity of the nanoclusters were assessed by computing the HOMO–LUMO energy gaps from orbital eigenvalues. Multiwfn packages were used to do orbital visualization based on the generated .molden files.

2.7 Molecular docking studies

2.7.1 Target protein retrieval and preparation. The crystal structure of *Bacillus cereus* (PDB ID: 1BMC),[6] *Candida albicans* (PDB ID: 6AKZ),[7] *E. coli* (PDB ID: 3ZMI),[8] *Salmonella typhi* (PDB ID: 6IAI),[9] and *Staphylococcus aureus* (PDB ID: 4QLO)[10] protein was retrieved in PDB format utilizing data from RCSB Protein Data Bank (**https://www.rcsb.org/**). This *Bacillus cereus* (PDB ID: 1BMC), protein is composed of 1 chains (A). A chain sequence length is 221 amino acid residues. The structure's resolution is 2.50 Å, with an R_{free} value: 0.330 (Depositor).[6] To prepare the protein for further study, we used the protein preparation wizard available in Pymol to eliminate hetero atom molecules, water molecules, and co-crystalized ligand to get clean Protein.[23] Protein was cleaned by Pymol default parameters and optimized using SPDBV 4.10.[24] Similarly all remaining microbial proteins were prepared using the mentioned softwares and packages.

2.8 Prediction of toxicity of nanoclusters

The toxicity profiles of two metal oxide nanocomposites—Cu_3NiO_4 and Cu_4O_4—were evaluated using the ProTox-3.0 web server, a widely accepted platform for computational toxicity prediction using ProTox-3.0.[25] The server integrates machine learning models trained on large datasets to predict various toxicity endpoints, including LD_{50} values, toxicity classes, hepatotoxicity, immunotoxicity, mutagenicity, and cytotoxicity.[26] The platform utilizes a consensus approach incorporating structural alerts, molecular similarity, and pharmacophore features to improve prediction accuracy.[27]

3. Result and discussion

The synthesized CuO and Ni–CuO nanoparticles were comprehensively characterized and their structural, morphological, chemical, antimicrobial, and electronic properties were

investigated in detail. The crystallographic structure, morphology, elemental composition, and chemical bonding were evaluated by X-ray diffraction (XRD), field emission scanning electron microscopy (FESEM), energy-dispersive X-ray spectroscopy (EDX), and Fourier-transform infrared (FTIR) spectroscopy, respectively. Additionally, the photocatalytic degradation of organic dye under visible light and the antibacterial activity against bacterial and fungal strains were systematically evaluated. To better link the experimental results with the electrical structural and electronic behavior at the atomic scale, Density Functional Theory (DFT) computations were performed. The combined findings provide a comprehensive understanding of how Ni doping affects CuO nanostructures' physicochemical and functional properties.

3.1 XRD analysis

The crystalline structure and phase purity of the synthesized CuO and Ni–CuO nanoparticles were analyzed using X-ray diffraction (XRD). The diffraction patterns, shown in Fig. 1(a), display sharp and well-defined peaks, indicating the high crystallinity of the samples. All prominent peaks of CuO sample were indexed to the monoclinic phase of CuO (JCPDS card no. 01-077-7716), corresponding to diffraction planes such as (110), (−111), (111), (−202), and (202) at 2θ values of approximately 32.5°, 35.5°, 38.7°, 45.5°, and 48.7°, respectively.[28] The absence of additional peaks confirms the phase purity of the synthesized product. Minor matching scores for oxygen-related phases (O_2 and O_3) were observed during phase identification; however, these scores were below the accepted significance threshold (score < 30). Moreover, no corresponding diffraction peaks were evident in the experimental patterns, suggesting these signals likely arose from background noise or instrumental artifacts. Consequently, these phases were excluded from further analysis. Upon Ni doping, the diffraction peaks remained consistent with the monoclinic CuO structure, indicating that the crystal system was preserved. However, slight peak broadening and

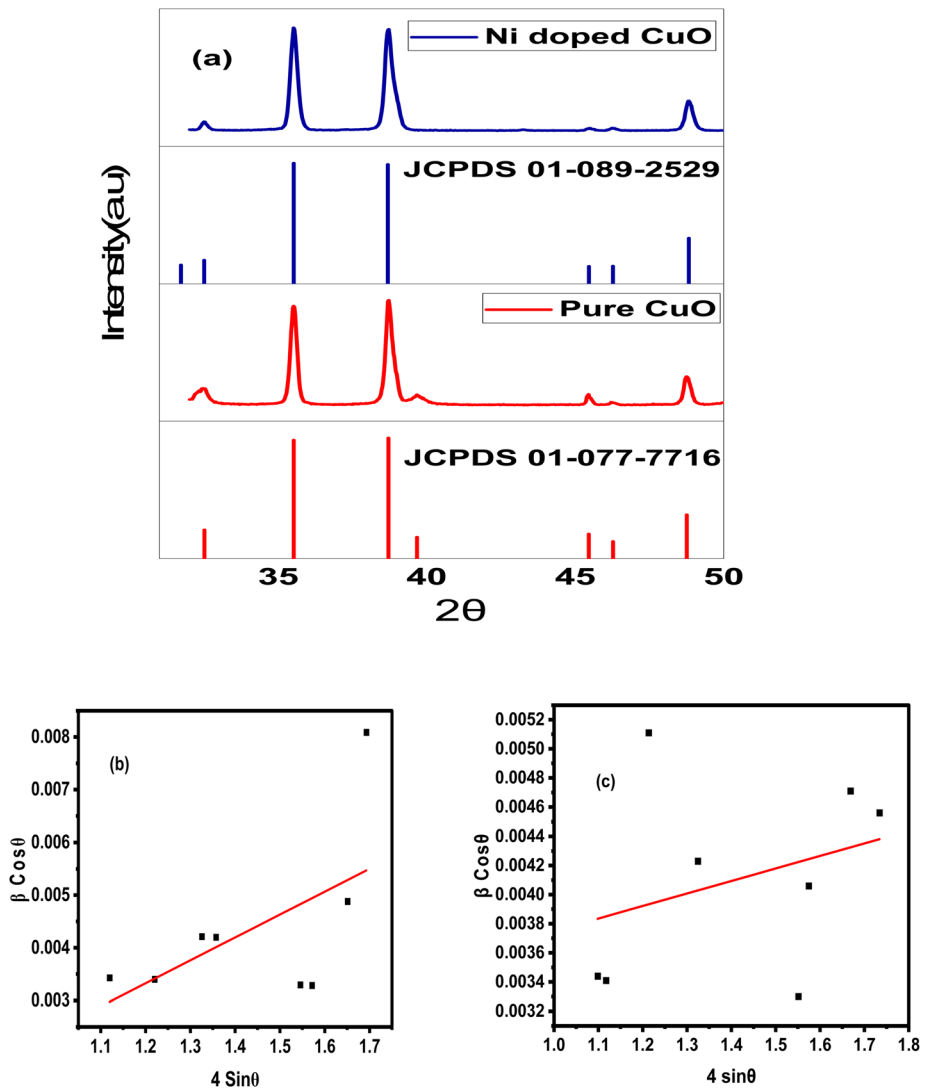

Fig. 1 (a) XRD patterns of pure and Ni-doped CuO nanoparticles, confirming the monoclinic CuO phase and indicating lattice contraction upon doping. (b) Williamson–Hall plots ($\beta \cos\theta$ *vs.* $4 \sin\theta$) showing size-strain separation for pure CuO (c) Ni doped CuO.

marginal shifts in the peak positions were observed, suggesting lattice distortion due to the incorporation of Ni^{2+} ions (ionic radius ~ 0.69 Å) into the Cu^{2+} lattice sites (ionic radius ~ 0.73 Å). Such substitution induces microstrain and local disorder in the crystal lattice. Crystallite sizes were initially estimated using the Scherrer equation, applied to the most intense diffraction peaks. The average crystallite size of CuO was found to be 32.91 nm, while that of Ni–CuO was reduced to 27.17 nm, indicating that Ni doping restricted crystal growth during the sol–gel synthesis process.[28,29] To decouple the effects of microstrain and size-induced broadening, the Williamson–Hall (W–H) method was employed. A plot of $\beta\cos\theta$ *versus* $4\sin\theta$ is shown in Fig. 1(b) and (c) from which crystallite size and lattice strain were extracted.[11] The W–H plot yielded a linear fit with intercepts of 0.00208 (CuO) and 0.00349 (Ni–CuO), and slopes of 0.00139 and 0.000763, respectively. Using the intercepts and the equation:

$$D = \frac{K\lambda}{\text{intercept}}$$

where $K = 0.9$ and $\lambda = 0.15406$ nm, the W–H crystallite sizes were calculated to be approximately 66.65 nm for CuO and 39.72 nm for Ni–CuO (Table 1). The slight discrepancy with the Scherrer values is expected, as W–H analysis accounts for both size and strain contributions to peak broadening, whereas the Scherrer equation assumes strain-free conditions.

The increased microstrain (ε) in the doped sample underscores lattice distortion due to Ni^{2+} incorporation, in agreement with literature.[28,29] Such distortions are expected to affect crystal growth and reactivity of CuO-based catalysts.

It should be noted that the linear regression yielded relatively low adjusted R^2 values indicating weak statistical reliability of the W–H fits. Such limitations are frequently reported in lightly doped oxide systems, where peak broadening is subtle and often dominated by instrumental factors rather than strain. Therefore, the W–H results here are considered as indicative trends rather than absolute values. The Scherrer equation, applied to the main diffraction peaks, provides more robust crystallite size estimates and is used as the primary basis for discussion.

Despite this limitation, the W–H analysis still suggests a relative increase in microstrain (ε) in the doped sample, which is consistent with lattice distortion arising from Ni^{2+} incorporation. Such distortions are reported to hinder crystal growth and modify the surface reactivity of CuO-based catalysts.[28,29]

3.2 Morphological analysis (FESEM and EDX)

Field Emission Scanning Electron Microscopy (FESEM) was utilized to investigate the surface morphology and particle distribution of both CuO and Ni–CuO nanoparticles. The FESEM images of CuO and Ni–CuO nanoparticles are shown in Fig. 2(a, c) and (b, d) respectively. Both samples exhibit quasi-spherical nanoparticles with varying degrees of agglomeration. The Ni–CuO sample appears more clustered with slightly rougher surface textures.[30,31] The images of pure and Ni–CuO nanoparticles reveal the morphological features including particle size and distribution at two different magnifications (200 nm and 1000 nm scale bars). As commonly observed in sol–gel synthesized metal oxide nanoparticles, some degree of particle agglomeration is present due to the high surface energy and strong interparticle interactions inherent in nano-sized materials. This agglomeration leads to particle clusters where individual nanoparticles become difficult to distinguish clearly on the micrographs. To address this, the samples were carefully prepared to improve dispersion before imaging, and multiple independent regions were analyzed using the ImageJ software to estimate particle size distribution. Despite the presence of agglomerates, the analysis focused on well-dispersed areas where primary particles could be identified more distinctly. Particle size distributions showed the majority of nanoparticles lie below 200 nm, which aligns well with the crystallite size values obtained from XRD analysis.[32]

Energy-Dispersive X-ray Spectroscopy (EDX) was employed to determine the elemental composition of the synthesized nanoparticles and to evaluate the effectiveness of Ni doping. For CuO sample, point analyses at two different regions (point 7 and point 8) and the representative spectrum (spectrum 4) revealed only copper (Cu) and oxygen (O), with atomic percentages of Cu: 50.41–44.65% and O: 49.59–55.35% (weight percentages: Cu: 76.22–80.15%, O: 19.85–23.78%). These results confirm the high purity of the CuO nanoparticles without detectable contamination. Representative EDX spectra for these points are presented in Fig. 3(a). For the Ni–CuO sample, EDX analysis at multiple points (points 9, 10, and spectrum 5) confirmed the successful incorporation of Ni into the CuO lattice. The measured atomic percentages were:

Point 9: Cu – 46.58%, O – 52.43%, Ni – 0.99%

Point 10: Cu – 51.71%, O – 46.85%, Ni – 1.44%

Spectrum 5: Cu – 44.31%, O – 55.07%, Ni – 0.62%

(weight percentages: Cu 75.42–79.76%, O 18.19–23.60%, Ni 0.98–2.05%). These consistent results across multiple points indicate effective doping and confirm the presence of Ni in the nanoparticles. Representative EDX spectra for the Ni–CuO sample are shown in Fig. 3(b). It is important to note that while EDX provides quantitative elemental composition, it cannot unambiguously confirm the homogeneous spatial distribution of Ni within the sample. However, the repeated detection of Ni at multiple points suggests uniform incorporation, in agreement with previously reported studies on Ni–CuO nanoparticles.[30,31]

Table 1 Comparison of crystallite size and microstrain of pure and Ni-doped CuO nanoparticles

Sample	Scherrer size (nm)	W–H size (nm)	Lattice strain ($\times10^{-3}$)
Pure CuO	32.91	66.65	1.39
Ni-doped CuO	27.17	39.72	0.763

3.3 FTIR analysis

FTIR spectroscopy was employed to analyze the functional groups and structural variations between pure and Ni–CuO nanoparticles (NPs), with spectra recorded in the range of 4000–400 cm^{-1} (Fig. 4). In the spectrum of CuO NPs (red curve), a broad band

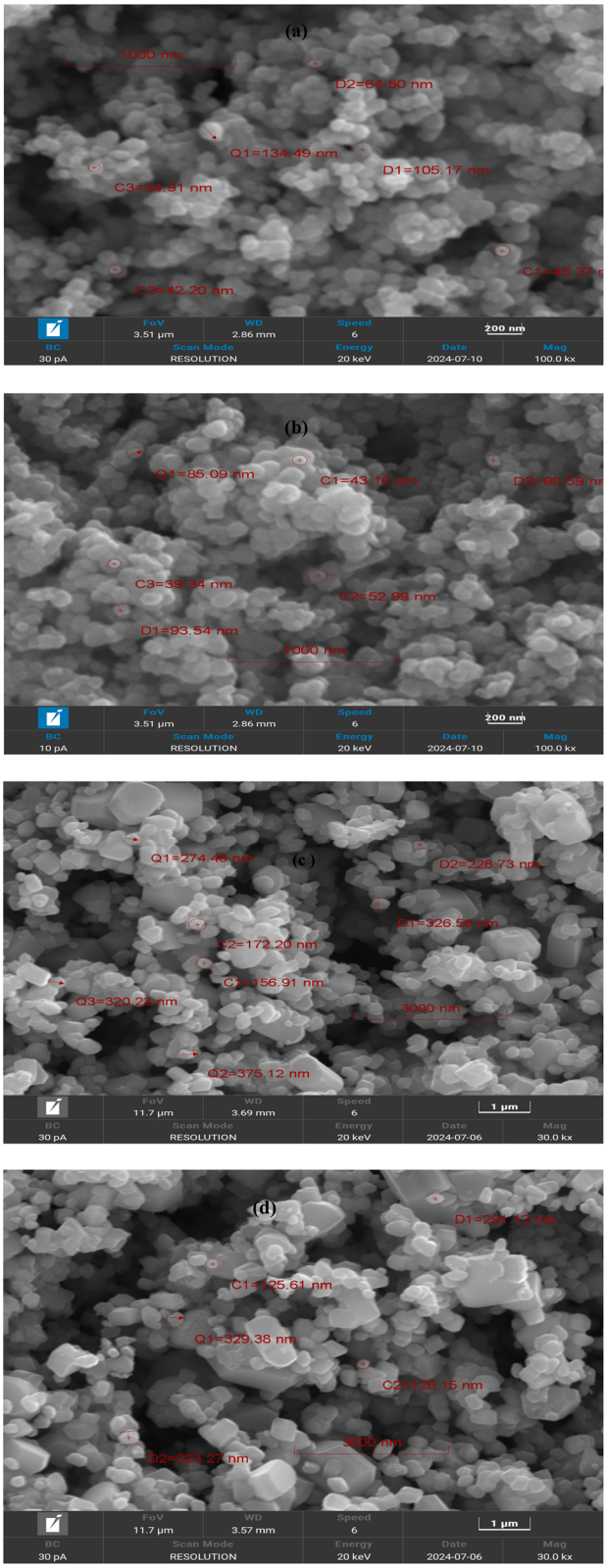

Fig. 2 (a) FESEM micrographs of pure and (b) Ni-doped CuO nanoparticles showing the quasi-spherical morphology at 200 nm. (c and d) Pure and Ni dope CuO at 1000 nm scale.

observed around 3400–3200 cm^{-1} corresponds to the O–H stretching vibrations of surface-adsorbed water or hydroxyl groups.[33,34] The peak near 1600–1400 cm^{-1} is attributed to H–O–H bending, further confirming the presence of moisture. A strong absorption band belongs to the Cu–O stretching vibrations around 500–600 cm^{-1}, which confirms the formation of copper oxide nanoparticles.[33,34] In the Ni–CuO sample (blue curve), similar bands are present but exhibit reduced intensity and slight shifts in position. The O–H stretching and H–O–H bending bands are less pronounced, indicating altered surface chemistry likely due to Ni^{2+} incorporation.[33] Notably, the Cu–O stretching region also shows a weakened and slightly shifted absorption, suggesting lattice distortion or substitution of Cu^{2+} by Ni^{2+} ions. While no distinct Ni–O vibrational band was observed (as Ni–O modes are often IR-inactive or overlap with Cu–O bands), subtle changes in the Cu–O stretching region suggest successful Ni incorporation into the CuO lattice, causing lattice distortion and modified bonding environments. These changes indicate that Ni^{2+} ions were successfully introduced into the CuO matrix, modifying its local structure and potentially influencing its electronic, photocatalytic, and antimicrobial behavior. The results are consistent with prior studies on transition metal doping in CuO, where peak shifts and intensity reduction were also observed as indicators of dopant incorporation.[11,31]

3.4 Photocatalytic activity

The photocatalytic degradation of methylene violet (MV) dye was assessed under UV light using pure and Ni–CuO nanoparticles as catalysts. Photodegradation experiments were performed at two MV concentrations (15 ppm and 20 ppm).[35] Prior to UV illumination, all samples were subjected to a 30 minute dark adsorption period to ensure surface–dye equilibrium, eliminating the contribution of initial adsorption from the subsequent kinetic analysis. Similar studies using CuO-based materials have reported MV degradation efficiencies over 80% under UV light.[35,36] The percentage degradation of MV dye was calculated directly from the change in absorbance at 584 nm using the equation:

$$\text{Degradation } (\%) = \frac{A_0 - A_t}{A_0} \times 100$$

where (A_0) is the initial absorbance before UV irradiation and (A_t) is the absorbance at time t. This approach is consistent with previous studies on CuO-based photocatalysts[35,36] and assumes a linear relationship between absorbance and concentration according to the Lambert–Beer law.

The change in absorbance over time at the characteristic wavelength of MV dye indicated the progression of the photocatalytic reaction. Among the samples, Ni–CuO at 20 ppm exhibited the highest degradation efficiency (88.62%) within 90 minutes of UV exposure, while CuO at 20 ppm achieved 84.92% under identical conditions. These results surpass earlier reports on bare CuO or CeO_2–CuO systems (64–93%) indicating that Ni doping enhances active site density and electron–hole separation.[36] At the lower dye concentration (15 ppm), Ni–CuO reached 82.01% degradation compared to 70.00% by CuO.

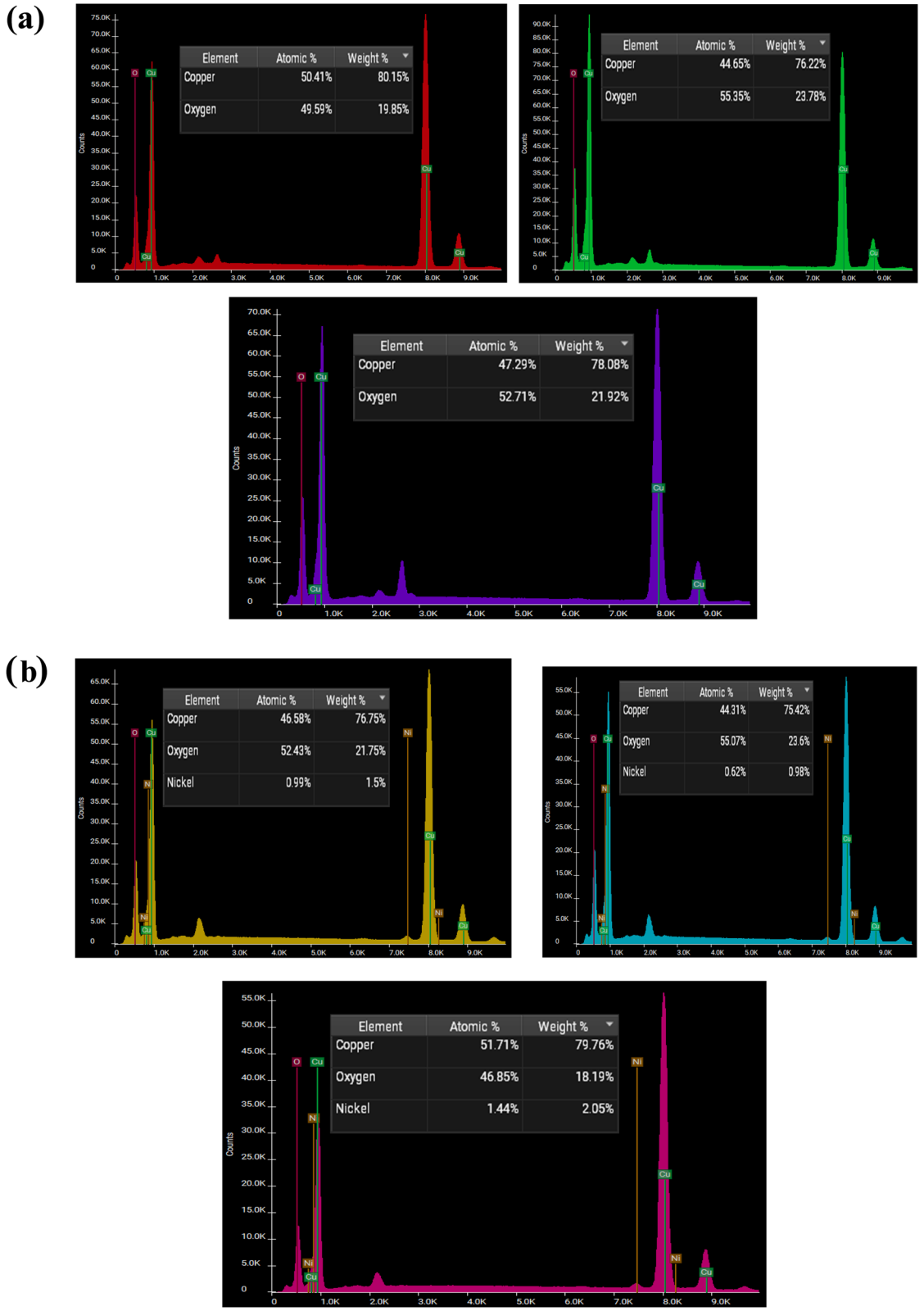

Fig. 3 EDX spectra of (a) pure CuO nanoparticles confirming the presence of Cu and O with near-stoichiometric distribution (point 7, 8 and spectrum 4). (b) EDX spectra of Ni-doped CuO nanoparticles (points 9, 10, spectrum 5). Representative EDX spectra showing elemental composition of pure and Ni-doped CuO nanoparticles. Ni is consistently detected across multiple points, supporting successful doping.

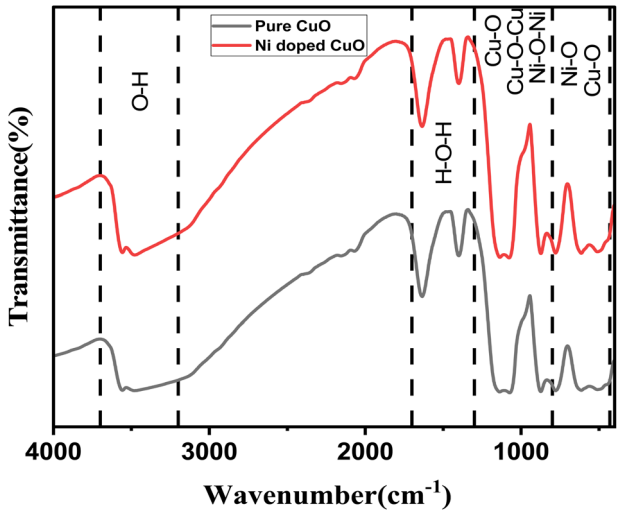

Fig. 4 FTIR spectra of pure and Ni-doped CuO nanoparticles.

The UV-Vis absorbance spectra of MV recorded at different time intervals using Ni–CuO 20 ppm are presented in Fig. 5(a). A gradual reduction in the absorption peak at ~584 nm confirms effective dye degradation under UV light.[35] The decrease in absorbance intensity as a function of time is illustrated in Fig. 5(b). The percentage degradation *versus* time for all samples, enabling a clear comparison of photocatalytic efficiencies are presented in Fig. 5(c).

To understand the reaction mechanism, the kinetics were fitted using a pseudo-first-order model described by:

$$\ln(A_0/A_t) = kt$$

where A_0 and A_t are the absorbance values at time zero and time t, respectively, and k is the apparent rate constant. The linear plots of $\ln(A_0/A_t)$ *versus* time for all four systems exhibited strong correlation ($R^2 > 0.95$), validating the pseudo-first-order reaction model (Fig. 5(d)). The rate constant (k) for Ni–CuO at 20 ppm was 0.02452 min^{-1}, slightly higher than that for CuO (0.02364 min^{-1}). At 15 ppm, Ni–CuO (0.00978 ± 0.00098 min^{-1}) significantly outperformed pure CuO (0.00547 ± 0.00055 min^{-1}), highlighting the effectiveness of Ni doping in enhancing the photocatalytic degradation rate at lower dye concentrations. The calculated half-life ($t_{1/2}$) values, derived from the rate constants using the equation:

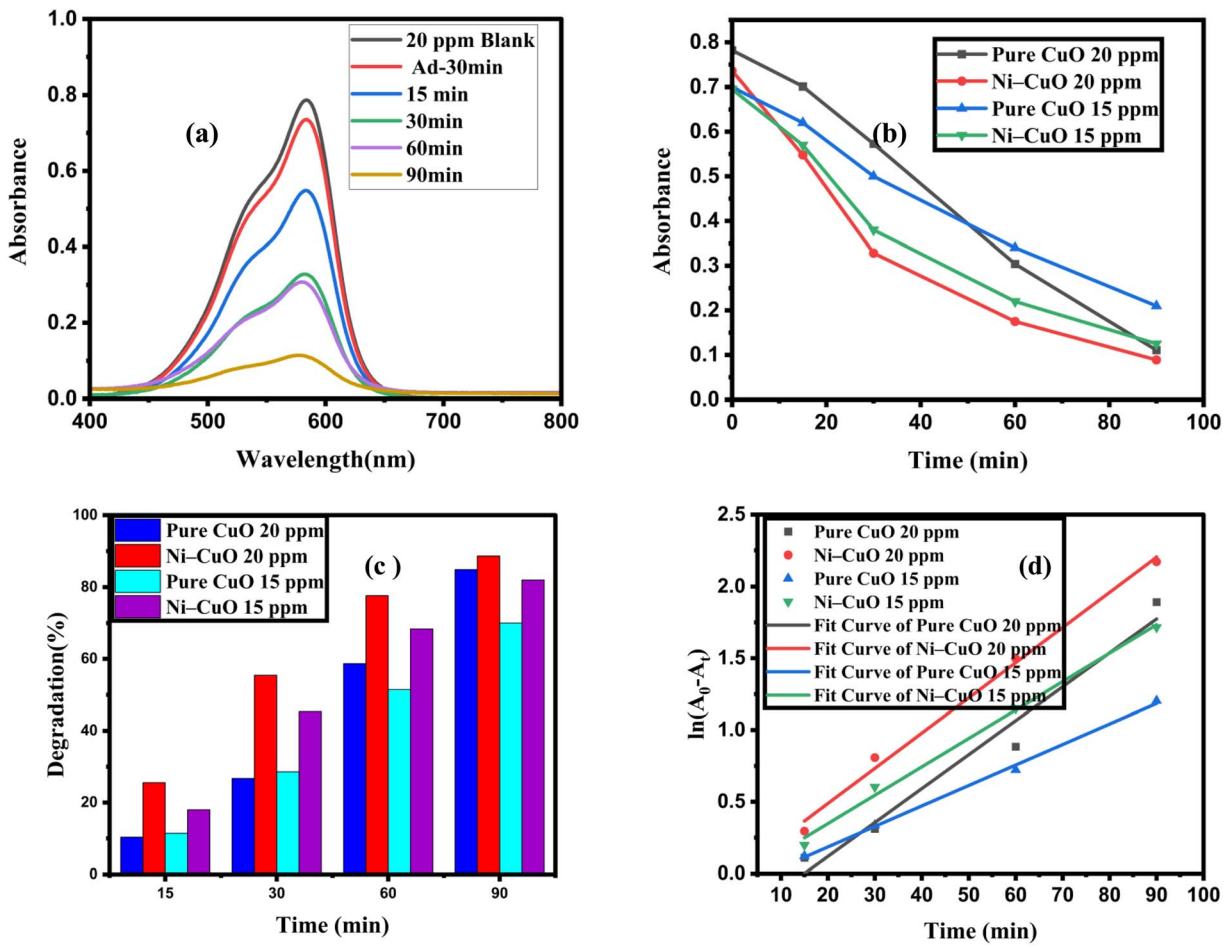

Fig. 5 (a) UV-Vis spectra of MV (20 ppm) during photocatalytic degradation using Ni–CuO under UV irradiation. The decrease in absorbance at λ_{max} (~584 nm) over time confirms dye breakdown. (b) Absorbance *versus* time profile for MV degradation under UV light. (c) Percentage degradation of MV as a function of irradiation time for all catalysts. (d) Pseudo-first-order kinetic plots of $\ln(A_0/A_t)$ *versus* time for Ni–CuO 20 ppm, pure CuO 20 ppm, Ni–CuO 15 ppm, and pure CuO 15 ppm.

Table 2 The corresponding kinetic parameters, including rate constants and half-lives

Sample	Rate constant k (min^{-1})	Half-life $t_{1/2}$ (min)	R^2
Ni–CuO 20 ppm	0.02452	28.26	0.99077
Pure CuO 20 ppm	0.02364	29.31	0.95285
Ni–CuO 15 ppm	0.00978	70.83	0.99271
Pure CuO 15 ppm	0.00547	126.65	0.99631

$$t_{1/2} = \frac{\ln(2)}{\kappa}$$

provide further insight into the degradation rate of MV dye.[35] A lower half-life indicates faster degradation. Among the catalysts, the calculated half-life ($t_{1/2}$) values showed that Ni–CuO required less time to degrade 50% of methylene violet than CuO at both 15 ppm and 20 ppm concentrations. At 15 ppm, the half-life of Ni–CuO was 70.83 minutes compared to 126.65 minutes for CuO, confirming enhanced photocatalytic efficiency due to Ni doping. TMatchewan optimized TiO_2-based catalysts achieving >95% degradation, with a clear kinetic trend described by pseudo-first-order behavior.[37] In our work, Ni–CuO showed a significantly higher rate (0.00978 min^{-1} at 15 ppm) compared to CuO (0.00547 min^{-1}), reflecting the positive impact of Ni doping. The corresponding kinetic parameters, including rate constants and half-lives, are summarized in Table 2.

It is well established that surface area and porosity strongly influence photocatalytic efficiency. While BET measurements were not performed in the current study, literature reports indicate that the synthesized CuO nanoparticles exhibit specific surface areas ranging from 12.4 $m^2 g^{-1}$ to 67.7 $m^2 g^{-1}$, higher than commercially available CuO NPs (1.38 $m^2 g^{-1}$), with type-IV isotherms characteristic of mesoporous materials with slit-like pores.[38] Similarly, mesoporous CuO nanoparticles with tunable size and morphology also demonstrate enhanced surface areas and porosity.[39] Furthermore, Ni-containing CuO-based composites, such as Cu–NiO@graphene microspheres, show significantly increased surface areas (~93 $m^2 g^{-1}$) and well-developed mesoporous structures.[40] This trend aligns with our observed photocatalytic activity, where Ni–CuO exhibited higher degradation rate constants and shorter half-lives than CuO. Increased surface area and porosity likely enhance dye adsorption and provide more active sites for electron–hole transfer, thereby accelerating degradation kinetics. Future work will include direct BET measurements and a systematic analysis of the correlation between pore structure parameters and photocatalytic performance to quantitatively strengthen the structure–activity relationship.

3.5 Antimicrobial activity

Ni–CuO and CuO nanoparticles were evaluated for antimicrobial activity against *Bacillus cereus*, *Escherichia coli*, *Staphylococcus aureus*, *Salmonella typhi*, and *Candida* at concentrations ranging from 50 to 250 μg mL^{-1}. Optical density (OD_{600}) measurements were used to quantify microbial growth inhibition. Data represent means ± SD of three replicates, and statistical significance between Ni–CuO and CuO was assessed by *t*-test ($p < 0.05$, $p < 0.01$). Complete data, including raw OD values and statistical analyses, are provided in Table S1.Both nanoparticles demonstrated significant, dose-dependent antimicrobial effects, with mean OD values decreasing as concentration increased (Table S1). Percentage inhibition, calculated as:

$$[(\text{Control OD} - \text{treatment OD})/\text{control OD}] \times 100$$

increased accordingly with concentration. At 250 μg mL^{-1}, pure CuO achieved percentage inhibitions of 91.7% ± 0.96 (*B. cereus*), 80.7% ± 1.12 (*E. coli*), 94.1% ± 0.88 (*S. aureus*), 76.8% ± 1.03 (*S. typhi*), and 98.4% ± 0.57 (*Candida*). Ni-doped CuO showed comparable or slightly enhanced activity, with inhibitions of 96.2% ± 0.44, 86.6% ± 0.96, 93.8% ± 0.92, 78.5% ± 1.02, and 99.7% ± 0.31 against the same pathogens (Table 3).Among all tested microbes, *Candida* was the most sensitive, exhibiting over 96% inhibition at concentrations of 100 μg mL^{-1} and above for both nanoparticles (Fig. 6(e)). Gram-positive bacteria (*S. aureus*, *B. cereus*) were generally more susceptible than Gram-negative bacteria (*E. coli*, *S. typhi*) a trend consistent with prior studies on CuO NPs.[41] While CuO exhibited slightly higher inhibition against *B. cereus* and *E. coli* at the highest concentration, Ni–CuO demonstrated marginally better activity against *S. aureus* and *Candida* at intermediate concentrations (Fig. 6). These findings align with recent reports indicating that Ni doping can improve CuO's antimicrobial

Table 3 Percentage inhibition of microbial growth by Ni-doped CuO and pure CuO nanoparticles

Pathogen	Material	50 μg mL^{-1}	100 μg mL^{-1}	150 μg mL^{-1}	200 μg mL^{-1}	250 μg mL^{-1}
B. cereus	Ni-doped CuO	82.26 ± 2.04	86.42 ± 1.56	89.02 ± 1.26	89.91 ± 1.16	96.22 ± 0.44
B. cereus	Pure CuO	80.27 ± 2.27	85.76 ± 1.64	88.13 ± 1.37	90.73 ± 1.07	91.69 ± 0.96
E. coli	Ni-doped CuO	73.23 ± 1.98	74.71 ± 1.63	77.08 ± 1.42	79.22 ± 1.29	86.65 ± 0.96
E. coli	Pure CuO	60.89 ± 2.11	66.75 ± 1.88	72.62 ± 1.47	73.30 ± 1.36	80.70 ± 1.12
S. aureus	Ni-doped CuO	74.93 ± 2.44	89.50 ± 1.47	90.19 ± 1.33	92.89 ± 1.11	93.78 ± 0.92
S. aureus	Pure CuO	81.42 ± 2.07	90.61 ± 1.33	91.51 ± 1.21	92.47 ± 0.94	94.13 ± 0.88
S. typhi	Ni-doped CuO	60.18 ± 1.76	74.20 ± 1.42	77.72 ± 1.19	77.99 ± 1.13	78.54 ± 1.02
S. typhi	Pure CuO	59.54 ± 1.83	65.71 ± 1.55	70.04 ± 1.37	70.77 ± 1.26	76.82 ± 1.03
Candida	Ni-doped CuO	76.17 ± 2.17	85.60 ± 2.01	97.16 ± 0.86	97.37 ± 0.88	99.72 ± 0.48
Candida	Pure CuO	67.45 ± 2.36	96.67 ± 0.91	96.88 ± 0.88	97.87 ± 0.77	98.44 ± 0.56

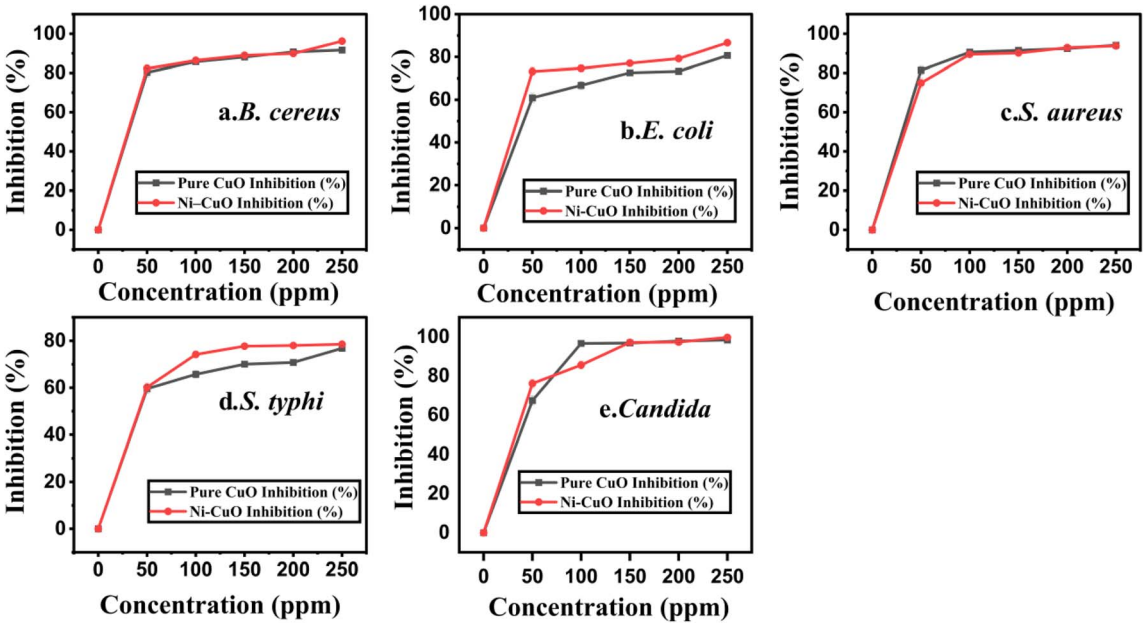

Fig. 6 Antimicrobial activity of pure CuO and Ni-doped CuO nanoparticles against (a) *B. cereus*, (b) *E. coli*, (c) *S. aureus*, (d) *S. typhi* and (e) *Candida* at 50–250 μg mL^{-1}. Percentage inhibition was calculated from OD_{600} readings. Data represent mean ± SD ($n = 3$). Both materials exhibited dose-dependent inhibition, with Ni-doped CuO showing superior efficacy in several cases.

activity, particularly against both Gram-positive and Gram-negative pathogens.[30] The underlying mechanisms likely involve enhanced Ni–O–Cu surface interactions and increased reactive oxygen species (ROS) generation, consistent with established CuO nanoparticle behavior.[42] Although both CuO and Ni–CuO nanoparticles exhibited strong antimicrobial activity, the enhancement from Ni doping was generally modest and pathogen-dependent. In particular, Ni–CuO showed slightly higher inhibition against *S. aureus* and *Candida* at intermediate concentrations, consistent with previous studies suggesting Ni incorporation can modulate antimicrobial performance.

3.6 DFT analysis and electronic properties

To gain insight into the electronic properties of the synthesized nanoclusters, density functional theory (DFT) calculations were performed on the optimized geometries of pure Cu_4O_4 (triplet spin state) and Cu_3NiO_4 (doublet spin state) clusters. To understand the local structural modifications induced by Ni doping in the Cu_4O_4 nanocluster, a detailed analysis of bond lengths and bond angles was conducted. The optimized geometry of Cu_4O_4 cluster revealed typical Cu–O bond lengths ranging from 1.85 Å to 2.32 Å, consistent with a distorted square planar coordination environment commonly observed in transition metal oxides. In the Ni-doped Cu_3NiO_4 cluster, the Ni–O bonds were slightly shorter (*e.g.*, 1.72 Å and 1.80 Å) compared to the corresponding Cu–O bonds, reflecting the higher electronegativity and smaller ionic radius of Ni^{2+} relative to Cu^{2+}. Additionally, selected bond angles such as ∠O–Ni–O (150.46°) and ∠Cu–O–Cu (54.24–87.87°) indicated minor angular distortions around the metal centers upon doping. A full list of computed bond lengths and bond angles for both pristine and doped nanoclusters, along with the optimized Cartesian coordinates and 3D structural visualizations, is provided in the SI (Tables S7, S8 and Fig. S4).The calculated HOMO–LUMO energy gap for Cu_4O_4 was 0.303 eV (α-spin) and 0.672 eV (β-spin), while Cu_3NiO_4 exhibited slightly larger gaps of 0.720 eV (α) and 0.735 eV (β) (provided in Table S2). This disparity is attributed to the spin multiplicity change restricting spin delocalization—a phenomenon highlighted in recent DFT studies of Cu_3NiO_4 systems.[43] Despite the increased gap in the doped system, Cu_3NiO_4 demonstrated superior photocatalytic and antimicrobial activity in experimental results (see Sections 3.4 and 3.5). The spatial distribution of the frontier molecular orbitals for both nanoclusters is illustrated in Fig. 7. For the pure Cu_4O_4 cluster, the α-HOMO is mainly localized over Cu atoms, while the α-LUMO shows delocalization across Cu and O atoms, suggesting potential for efficient charge transfer. In the Cu_3NiO_4 cluster, Ni substitution leads to a notable redistribution of orbital densities, with the α-HOMO and α-LUMO exhibiting enhanced overlap with surrounding oxygen atoms, potentially facilitating improved charge separation and surface reactivity. These orbital features support the enhanced photocatalytic and antimicrobial performance observed experimentally for the Ni-doped system (Sections 3.4 and 3.5).[40] while further analysis of electronic structure is presented in Section 4.

To understand the influence of Ni doping on charge redistribution within the Cu_4O_4 nanocluster, a comprehensive population analysis was conducted using the Hirshfeld, Mulliken, and Löwdin charge schemes. Among these, the Hirshfeld method was selected for primary discussion due to its reduced basis set dependency, improved numerical stability, and physically realistic description of charge localization—especially in

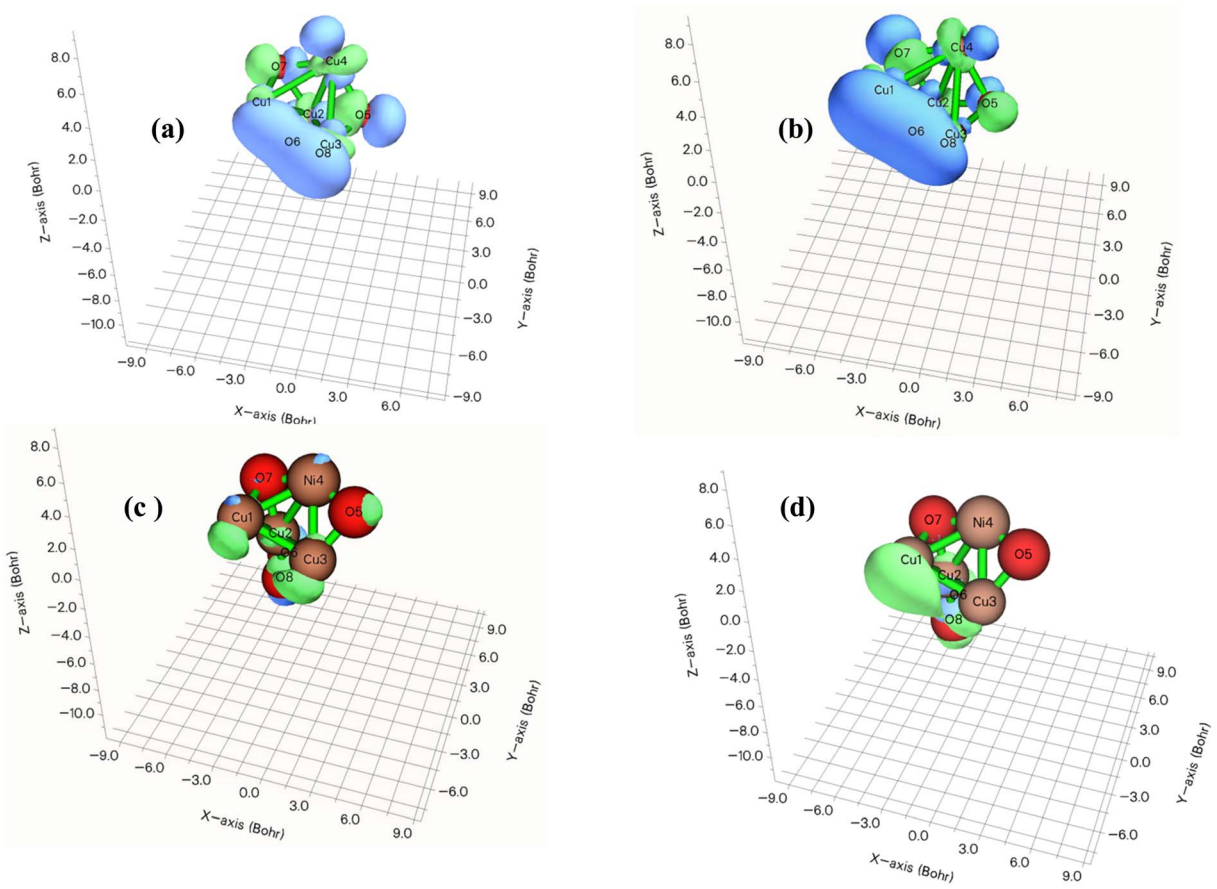

Fig. 7 Frontier molecular orbitals of the nanoclusters calculated at the DFT level (B3LYP/def2-SVP, spin-unrestricted). (a) α-HOMO of pure Cu_4O_4 (triplet), (b) α-LUMO of pure Cu_4O_4 (triplet), (c) α-HOMO of Ni–Cu_3O_4 (doublet), (d) α-LUMO of Ni–Cu_3O_4 (doublet).

systems involving transition metals. The resulting atomic charges are summarized in Table 4 for both the pristine Cu_4O_4 and the Cu_3NiO_4 nanoclusters. In the undoped Cu_4O_4 cluster, the Cu atoms exhibited positive partial charges ranging from +0.2599 to +1.1184 a.u., while the O atoms carried negative charges between −0.1526 and −1.0241 a.u., consistent with strong ionic character in Cu–O bonding. Upon substitution of one Cu atom by Ni, a notable redistribution of electron density occurred. The Ni dopant exhibited a charge of +0.5596 a.u., which is significantly lower than the most oxidized Cu site in the undoped cluster, suggesting distinct electronic behavior.

Table 4 The Hirshfeld atomic charges are summarized for both the pristine Cu_4O_4 and the Ni-doped Cu_3NiO_4 nanoclusters

Atom	Element	Cu_4O_4 (charge, a.u.)	Cu_3NiO_4 (charge, a.u.)
1	Cu	0.2974	0.3328
2	Cu	1.1184	0.7574
3	Cu	0.2599	0.3363
4	Cu/Ni	0.7321	+0.5596(Ni)
5	O	−0.9654	−0.6884
6	O	−0.1526	−0.142
7	O	−1.0241	−0.8783
8	O	−0.2657	−0.2775

The remaining Cu atoms in the doped system carried charges between +0.3328 and +0.7574 a.u., and the O atoms exhibited slightly less negative charges (from −0.1420 to −0.8783 a.u.) compared to those in the pure cluster. This shift in charge distribution indicates that Ni incorporation reduces the polarization of Cu–O bonds, potentially promoting greater electronic delocalization and influencing the material's catalytic or electronic properties. To provide a broader view of the electronic structure, Mulliken and Löwdin charge analyses were also performed (see Tables S3–S6 in the SI). While overall trends such as charge transfer from metals to oxygen and reduction in O atom polarization upon Ni doping were consistent, quantitative differences were noted. For instance, Löwdin charges generally showed lower polarization, while Mulliken analysis exhibited slightly higher charge separation, especially at the Ni site.[44] These variations highlight the sensitivity of these methods to the basis set and justify the emphasis on Hirshfeld results for core interpretation.

The TDOD, PDOS, OPDOS profiles of Cu_4O_4 and Cu_3NiO_4 nanoclusters, as shown in Fig. 8(a) and (b), exhibit distinct electronic features. In the pure system (Fig. 8(a)), the density of states near the HOMO–LUMO edges is primarily derived from Cu 3d and O 2p orbitals.[45] In contrast, the Ni-doped cluster (Fig. 8(b)) displays additional states close to the Fermi level due to Ni 3d

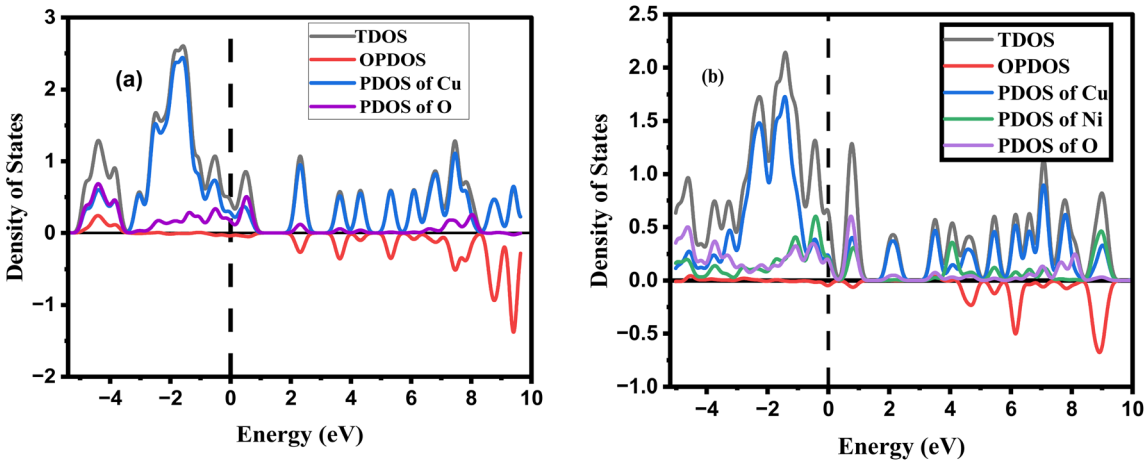

Fig. 8 Projected density of states (PDOS) for (a) Ni-doped Cu_3NiO_4 and (b) pure Cu_4O_4 nanoclusters. The Fermi level is set at 0.00 eV (dashed vertical line). The individual contributions of Cu 3d, O 2p, and Ni 3d orbitals are shown. Ni doping introduces new electronic states near the Fermi level and indicates orbital hybridization with surrounding atoms.

orbital contributions. These newly introduced states slightly shift the valence and conduction band edges, effectively reducing the HOMO–LUMO energy gap. Furthermore, the appearance of orbital overlap density of states (OPDOS) in the doped system suggests increased hybridization and electronic delocalization, potentially enhancing the catalytic activity of the material.

Although direct photocurrent and electrochemical impedance spectroscopy (EIS) measurements were not performed in this study, previous reports have shown that Ni incorporation significantly reduces charge transfer resistance in CuO systems.[46,47] For instance, these studies demonstrated that Ni doping enhances charge transfer properties, leading to improved photocatalytic efficiency. These findings suggest that Ni doping promotes more efficient separation and transport of photogenerated electron–hole pairs, aligning with the trends observed in our DFT analysis. The redistribution of frontier orbitals and decreased polarization of metal–oxygen bonds in Cu_3NiO_4 clusters imply enhanced electronic delocalization, which may facilitate improved charge carrier mobility and reduced recombination rates. Future work will include experimental photocurrent and EIS measurements to quantitatively validate these predictions and provide a more comprehensive understanding of the charge dynamics in these nanoclusters.

3.7 Photocatalytic mechanism of Ni–CuO (Cu_3NiO_4)

The proposed photocatalytic mechanism of Ni–CuO (Cu_3NiO_4) under UV illumination ($\lambda \approx 365$ nm) is illustrated in Fig. 9. Upon irradiation, photons with energy greater than or equal to the band gap (E_9) are absorbed by the Cu_3NiO_4 catalyst, resulting in the excitation of electrons from the valence band (VB) to the conduction band (CB), leaving behind corresponding holes (h^+) in the VB, as represented by:

$$Cu_3NiO_4 + h\nu \rightarrow e_{CB}^- + h_{VB}^+$$

The VB is primarily composed of O 2p orbitals, whereas the CB mainly arises from hybridized Cu 3d and Ni 3d orbitals. Incorporation of Ni^{2+} ions into the CuO lattice slightly narrows the band gap and introduces localized energy states between the VB and CB, thereby facilitating electron excitation and improving visible-light responsiveness.

Density functional theory (DFT) and XRD analyses confirm that Ni^{2+} ions substitute Cu^{2+} within the lattice, forming Ni–O bonds of approximately 1.72 Å. The substitution introduces shallow donor levels near the CB, which enhances charge carrier separation and migration. DFT orbital overlap analysis further suggests that Ni incorporation increases the degree of charge delocalization, effectively suppressing electron–hole (e^-–h^+) recombination.

Following photoexcitation, the photogenerated electrons (e^-) migrate toward the catalyst surface *via* Ni sites, while the corresponding holes (h^+) remain in the O 2p-derived valence band. These charge carriers participate in surface redox reactions according to the following pathways:

$$e_{CB}^- + O_2 \rightarrow {}^{\bullet}O_2^-$$

$$h_{VB}^+ + H_2O \rightarrow {}^{\bullet}OH + H^+$$

The resulting reactive oxygen species (ROS), including superoxide ($^{\bullet}O_2^-$) and hydroxyl radicals ($^{\bullet}OH$), play dominant roles in the oxidative degradation of organic pollutants.[48,49]

Methyl Violet (MV, $C_{14}H_{12}N_3SO_3$) molecules are preferentially adsorbed near Ni-enriched regions of the Cu_3NiO_4 surface, as indicated by the DFT-calculated adsorption energy (ΔE_{ads}). Stronger MV–Ni–O interactions promote enhanced dye binding and proximity to reactive centers, facilitating efficient photodegradation. The ROS produced subsequently attack the dye molecules, leading to stepwise oxidation and mineralization into CO_2, H_2O, and inorganic ions:

$$MV + ({}^{\bullet}OH/{}^{\bullet}O_2^-) \rightarrow \text{intermediates} \rightarrow CO_2 + H_2O + \text{mineral salts.}$$

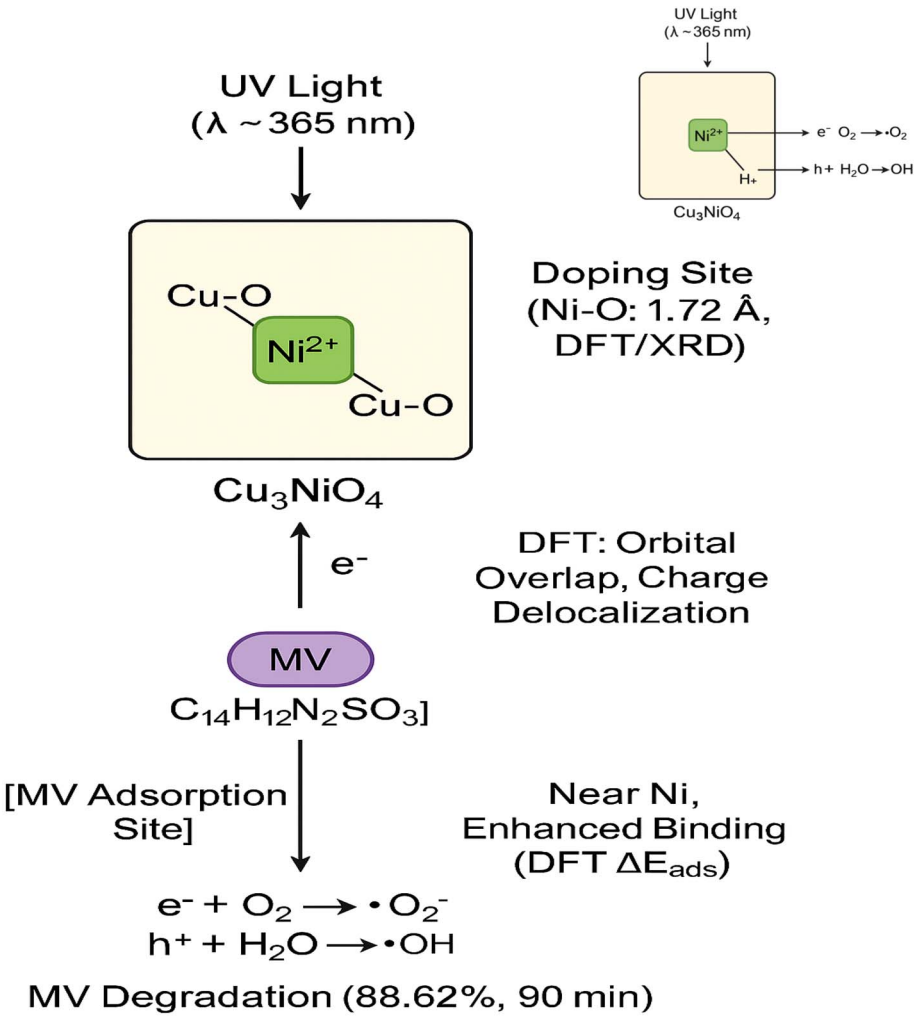

Fig. 9 Schematic illustration of the photocatalytic mechanism of Cu_3NiO_4 under UV irradiation ($\lambda \approx 365$ nm). Photon absorption promotes electron excitation from the O 2p valence band to the Cu/Ni 3d conduction band, while Ni^{2+} doping enhances charge separation and reduces recombination. The generated $^{\bullet}O_2^-$ and $^{\bullet}OH$ radicals oxidize Methyl Violet (MV) into CO_2 and H_2O, achieving 88.62% degradation within 90 min.

3.8 Analysis of molecular docking and evaluation of P-L interactions

Using PyRx software, molecular docking was performed on Cu_4O_4 and Cu_3NiO_4 against the target microbial proteins. Between these two ligands, the second one (Ni-doped nanoparticles) emerged as the best candidate against *E. coli* (binding score: −5.5 kcal mol^{-1}), *S. typhi* (binding score: −5 kcal mol^{-1}), and *Candida* (binding score: −5 kcal mol^{-1}), indicative of their strong potential for interaction. On the contrary, the first one, Cu_4O_4, which was docked against all with the aforementioned microbial proteins, and Cu_4O_4 works as the best candidate against *Candida* (binding score −4.8 kcal mol^{-1}) (Fig. 10).

Molecular interactions between ligands (Cu_4O_4 and Cu_3NiO_4) and receptors were visualized using Biovia Discovery Studio Visualizer.[50] Different types of interactions were involved, such as hydrophobic bonds, polar bonds, and hydrogen bonds. Specifically there are 3 types of intermolecular bonds are present like conventional hydrogen bond, metal-acceptor, and Pi–sulfur bonds. In the process of molecular docking these two nanoclusters, exhibited interaction with specific amino acid residues shared by the protein. The common amino acid involved in conventional H-bonding comprises ARG254. Furthermore, THR248, GLU234, and ARG254 take part in metal-acceptor type non-bonding interaction. Additionally, amino acid CYS250 was found to participate commonly in Pi–S bonding. Notably, each of the two nanoparticles displayed a unique interaction pattern with a distinct amino acid residue as illustrated in Fig. 11 detailed in SI (Fig. S1–S3). These interactions between amino acid residues with different portion of ligands stabilize the protein ligand complex.[51] In the molecular docking of both clusters against five microbial proteins, Cu_4O_4 & Cu_3NiO_4 nanoclusters both showed the highest inhibition against *Candida* (PDB ID: 6AKZ) which is aligned with our experimental data.

According to ProTox-3.0 predictions, Cu_4O_4 demonstrated a relatively safer toxicity profile than Cu_3NiO_4. The predicted LD_{50} for Cu_3NiO_4 was significantly lower (~255 mg kg^{-1}), categorizing it in Toxicity Class 3 (toxic if swallowed), while Cu_4O_4

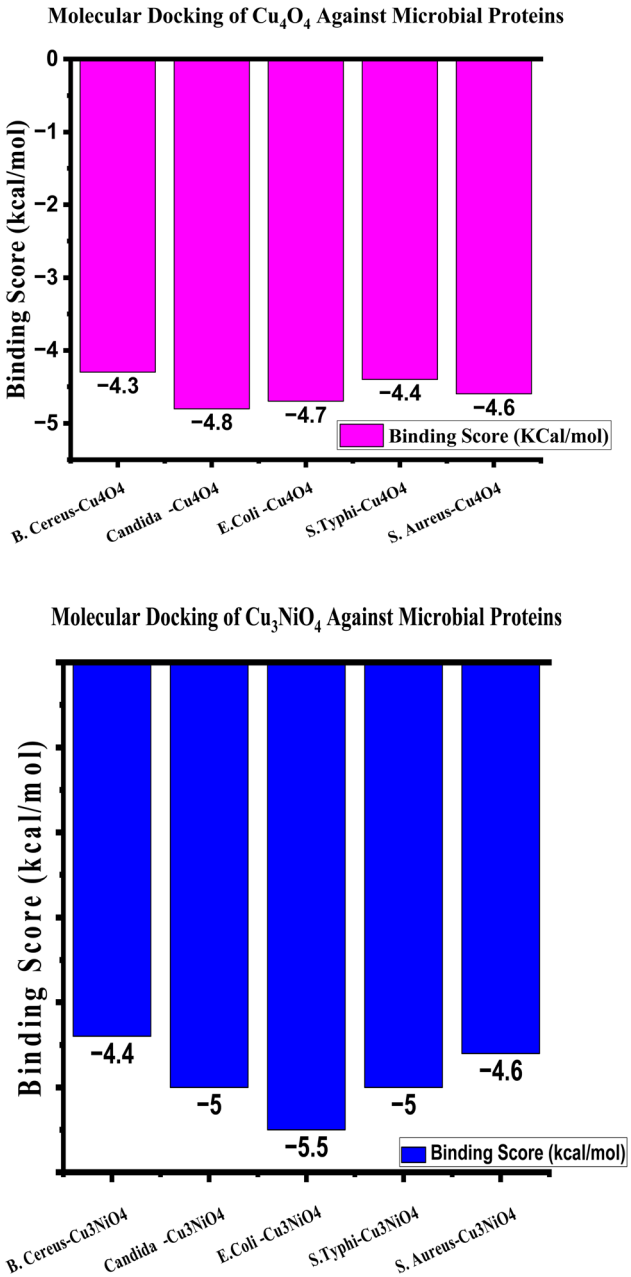

Fig. 10 Molecular docking score of Cu_4O_4 and Cu_3NiO_4 against 5 microbial proteins.

showed a higher LD_{50} (~1950 mg kg^{-1}), placing it in Toxicity Class 4 (harmful if swallowed).[26]

In terms of hepatotoxicity, Cu_3NiO_4 was flagged as active, suggesting potential liver damage upon prolonged exposure, whereas Cu_4O_4 was predicted to be inactive, indicating a lower hepatic risk.[52] This result aligns with previous findings on the toxic influence of transition-metal-doped copper oxides on hepatic biomarkers *in vivo*.[53]

For immunotoxicity, Cu_3NiO_4 again showed active response, suggesting potential immunosuppressive effects, whereas Cu_4O_4 was classified as inactive, implying minimal risk to immune function. Such immunotoxic responses are often

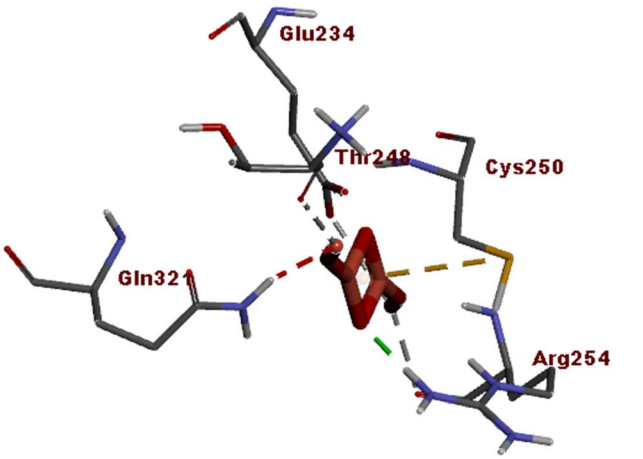

Fig. 11 Non-bonding interactions of Cu_4O_4 cluster against (a) 6AKZ (pose predicted by AutoDock Vina).

attributed to nickel's immunomodulatory potential, which is known to interfere with cytokine signaling and lymphocyte activation.[54]

Interestingly, neither compound was predicted to be mutagenic, indicating a low likelihood of DNA-damaging effects. This prediction is particularly crucial for biomedical applications, where genetic safety is essential.[55]

On cytotoxicity, both compounds showed active responses, although the score for Cu_3NiO_4 was more severe, reaffirming the additional toxicity burden introduced by nickel incorporation.[56]

These findings suggest that while both nanomaterials exhibit some degree of toxicity, Cu_4O_4 appears safer for biomedical or environmental applications due to its lower hepatotoxic and immunotoxic risk profiles. The substitution of nickel in the copper oxide lattice, while enhancing catalytic properties, seems to increase the compound's biological risks. Therefore, careful optimization is essential when designing such nanocomposites for real-world applications.[9]

3.9 Correlation between experiment and theory

The theoretical findings obtained from DFT calculations strongly align with the experimental characterizations, reinforcing the reliability of the predicted properties of both the pure Cu_4O_4 and Ni-doped Cu_3NiO_4 nanoclusters.

Structurally, the optimized geometries revealed that the Ni–O bonds in the doped cluster (1.72–1.80 Å) are shorter than the Cu–O bonds in the pure cluster (1.85–2.32 Å), which correlates well with the XRD results that showed peak shifts toward higher 2θ values upon Ni doping (see Fig. 1(a)). This shift indicates lattice contraction, consistent with the smaller ionic radius of Ni^{2+} compared to Cu^{2+}. Additionally, broader XRD peaks in the doped sample may be attributed to local symmetry distortions, which are reflected in the DFT-calculated bond angles—for example, a significantly large ∠O–Ni–O angle of 150.46° compared to more constrained Cu–O–Cu angles in the undoped structure (*e.g.*, 54.24–87.87°).

Charge distribution analysis using Hirshfeld, Mulliken, and Löwdin schemes showed a more balanced and less polarized

charge distribution in the doped system. This theoretical observation is corroborated by the EDX spectra (see Fig. 3(a) and (b)), confirming successful substitution of Cu by Ni, and by FTIR analysis (see Fig. 4), which exhibited minor shifts in Cu–O vibrational regions — indicating subtle but real modifications in the metal–oxygen bonding environment.

Interestingly, the HOMO–LUMO energy gap was found to be slightly higher in the Ni-doped Cu_3NiO_4 cluster (in doublet state) compared to the pure Cu_4O_4 cluster (in triplet state), contrary to the common expectation that doping reduces the gap. This counterintuitive result is justified by the difference in spin multiplicity: the doublet state restricts spin delocalization, resulting in orbital stabilization and a widened gap.[57] Despite this, the PDOS plots (Fig. 8) reveal that Ni doping introduces new Ni 3d states and alters orbital contributions near the Fermi level, enhancing orbital hybridization and charge carrier delocalization, which improve photocatalytic performance.[58]

Experimentally, Ni–CuO exhibited significantly enhanced photocatalytic degradation efficiency for methylene violet under UV light.[59–61] The theoretical insights into orbital interactions and reduced electron–hole recombination—as supported by overlapping PDOS and OPDOS features—provide a clear mechanistic basis for this improvement. Moreover, the enhanced orbital overlap and stronger Ni–O bonding predicted in the DFT model are likely contributors to more efficient reactive oxygen species (ROS) generation, in line with the observed superior antimicrobial activity of the Cu_3NiO_4 cluster.[58]

Overall, the strong agreement between structural, electronic, and reactive characteristics predicted by theory and observed experimentally validates the conclusion that Ni doping in CuO nanoclusters induces synergistic structural and electronic modifications, making it a promising strategy for tuning catalytic and antimicrobial properties.

4. Conclusion

This comprehensive investigation combined experimental and theoretical approaches to elucidate the structural, electronic, photocatalytic, and antimicrobial properties of pure Cu_4O_4 and Ni-doped Cu_3NiO_4 nanoclusters. The successful synthesis of both nanoclusters was confirmed by XRD, FESEM, EDX, and FTIR analyses, revealing notable changes upon Ni doping. XRD peak shifts toward higher 2θ values and bond length shortening (1.72–1.80 Å for Ni–O *vs.* 1.85–2.32 Å for Cu–O) reflected lattice contraction due to the smaller ionic radius of Ni^{2+}. FTIR spectra further supported altered bonding environments through minor shifts in metal–oxygen vibrational frequencies.

Photocatalytic studies demonstrated that Ni–CuO achieved a higher degradation efficiency of methylene violet (88.62% at 20 ppm in 90 minutes) and exhibited a faster degradation rate with a lower half-life (28.26 min) compared to CuO (84.92%, 29.31 min). Kinetic analysis validated the pseudo-first-order reaction model ($R^2 > 0.95$), and improved performance was particularly evident at low dye concentration (15 ppm), where the Ni-doped catalyst's rate constant was nearly double that of the undoped.

Antimicrobial assays showed that both nanoparticles possess strong dose-dependent activity, with Ni-doped CuO displaying slightly superior inhibition against certain strains. At 250 μg mL^{-1}, Ni–CuO inhibited *Candida* growth by 99.72% and showed robust activity against both Gram-positive and Gram-negative pathogens. Molecular docking and antimicrobial assays together highlighted the enhanced bioactivity of Ni-doped Cu_3NiO_4 over pure Cu_4O_4. Docking results showed stronger binding affinities of the doped nanocluster to microbial proteins from *E. coli*, *S. typhi*, and *Candida albicans*, with key interactions involving residues such as ARG254, THR248, and GLU234. These findings aligned with *in vitro* data, where Ni-doped CuO exhibited superior inhibition, especially against *Candida*. The combined *in silico* and experimental evidence supports the potential of Ni-doped CuO as a promising antimicrobial candidate, warranting further mechanistic and safety evaluations.

DFT calculations provided a deeper understanding of the observed phenomena. Despite exhibiting a slightly larger HOMO–LUMO gap in the doublet state, the Cu_3NiO_4 cluster featured enhanced orbital overlap and charge delocalization, as indicated by TDOS, PDOS and OPDOS analysis. Population analysis (Hirshfeld, Mulliken, and Löwdin) revealed less polarized and more balanced charge distribution after doping, aligning with experimental observations of enhanced conductivity and activity. Structural distortion and shorter Ni–O bonds contributed to the improved performance by facilitating faster charge transfer and stronger metal–oxygen hybridization.

Theoretical predictions strongly correlated with experimental outcomes, validating the synergistic impact of Ni doping in modulating geometry, electronic structure, and reactivity. This work underscores the potential of Ni–CuO nanoclusters as multifunctional materials for photocatalysis and antimicrobial applications, and establishes a valuable framework for rational design of doped transition-metal oxides in future studies. Although BET surface area analysis was not performed in this study, previous reports suggest that Ni–CuO nanoparticles generally possess a larger surface area than pure CuO, which could be one of the reasons behind their enhanced photocatalytic performance. In future work, direct BET measurements will be carried out to establish a clearer connection between surface characteristics and catalytic activity. Likewise, photocurrent response and electrochemical impedance spectroscopy (EIS) analyses will be included to quantitatively evaluate charge carrier separation and support the DFT predictions. Recent studies have also shown that Ni doping tends to lower charge transfer resistance and improve photocurrent response in CuO-based systems.

Conflicts of interest

There are no conflicts to declare.

Data availability

All data generated or analyzed during this study are included in this published article and its supplementary information (SI).

Supplementary information: additional figures, tables, and experimental details. See DOI: https://doi.org/10.1039/d5ra06284e.

References

1 S. Naz, A. Gul, M. Zia and R. Javed, Synthesis, biomedical applications, and toxicity of CuO nanoparticles, *Appl. Microbiol. Biotechnol.*, 2023, **107**(4), 1039–1061, DOI: 10.1007/s00253-023-12364-z.

2 S. Faisal, *et al.*, Curcuma longa mediated synthesis of copper oxide, nickel oxide and Cu-Ni bimetallic hybrid nanoparticles: Characterization and evaluation for antimicrobial, anti-parasitic and cytotoxic potentials, *Coatings*, 2021, **11**(7), 1–22, DOI: 10.3390/coatings11070849.

3 N. Khlifi, C. Zerrouki, N. Fourati, H. Guermazi, and S. Guermazi, Undoped and Ni/Fe doped CuO nanoparticles: A structural, optical, and photocatalytic comparative study, *9th EnvIMEKO Symp. Environ. Instrum. Meas. EnvIMEKO 2022*, 2022, pp. 24–29, DOI: 10.21014/10.21014/tc19-2022.05.

4 M. Bin Mobarak, M. F. Sikder, K. S. Muntaha, S. Islam, S. M. F. Rabbi and F. Chowdhury, Plant extract-mediated green-synthesized CuO nanoparticles for environmental and microbial remediation: a review covering basic understandings to mechanistic study, *Nanoscale Adv.*, 2025, **7**(9), 2418–2445, DOI: 10.1039/d5na00035a.

5 M. H. N. Assadi and D. A. H. Hanaor, The effects of copper doping on photocatalytic activity at (101) planes of anatase TiO_2: A theoretical study, *Appl. Surf. Sci.*, 2016, **387**(101), 682–689, DOI: 10.1016/j.apsusc.2016.06.178.

6 A. A. Gharib, M. I. A. El-Hamid, N. K. A. El-Aziz, E. Y. Yonan and M. O. Allam, Bacillus cereus: Pathogenicity, Viability and Adaptation, *Adv. Anim. Vet. Sci.*, 2020, **8**(1), 34–40, DOI: 10.17582/journal.aavs/2020/8.s1.34.40.

7 J. Talapko, *et al.*, Candida albicans: factores de virulencia y manifestaciones clínicas de la infección, *J. Fungi*, 2021, **7**(2), 1–19.

8 M. Basavaraju and B. S. Gunashree, Escherichia coli: An Overview of Main Characteristics, *Escherichia coli - Old New Insights*, 2023, DOI: 10.5772/intechopen.105508.

9 F. Rehman, A. M. Tareen, K. Taj and S. U. Khan, A Comprehensive Review on Salmonella Typhi: Pathogenesis, Clinical Features and Antibiotic Resistance Patterns, *Pak-Euro J. Med. Sci.*, 2023, **4**(1), 172–180, https://www.readersinsight.net/pjmls.

10 G. Gherardi, Staphylococcus aureus Infection: Pathogenesis and Antimicrobial Resistance, *Int. J. Mol. Sci.*, 2023, **24**(9), 8182, DOI: 10.3390/ijms24098182.

11 M. Chandrasekar, *et al.*, Synthesis and characterization studies of pure and Ni doped CuO nanoparticles by hydrothermal method, *J. King Saud Univ., Sci.*, 2022, **34**(3), 101831, DOI: 10.1016/j.jksus.2022.101831.

12 S. Al-Amri, *et al.*, Ni Doped CuO Nanoparticles: Structural and Optical Characterizations, *Curr. Nanosci.*, 2014, **11**(2), 191–197, DOI: 10.2174/15734137106661410242128 56.

13 L. Gontrani, *et al.*, CuO Nanoparticles and Microaggregates: An Experimental and Computational Study of Structure and Electronic Properties, *Materials*, 2023, **16**(13), 4800, DOI: 10.3390/ma16134800.

14 S. M. Jabbar, Synthesis of CuO Nano structure via Sol-Gel and Precipitation Chemical Methods, *Al-Khwarizmi Eng. J.*, 2017, **12**(4), 126–131, DOI: 10.22153/kej.2016.07.001.

15 Z. Singh and I. Singh, CTAB Surfactant Assisted and High pH Nano-Formulations of CuO Nanoparticles Pose Greater Cytotoxic and Genotoxic Effects, *Sci. Rep.*, 2019, **9**(1), 1–13, DOI: 10.1038/s41598-019-42419-z.

16 A. S. Jabur and A. D. Ahmed, Preparation and Evaluation of CuO Nanoparticles Using the Sol-Gel Method, *IOP Conf. Ser.: Mater. Sci. Eng.*, 2020, **987**(1), 3–8, DOI: 10.1088/1757-899X/987/1/012026.

17 A. Merah, A. Abidi, H. Merad, N. Gherraf, M. Iezid and A. Djahoudi, Comparative Study of the Bacteriological Activity of Zinc Oxide and Copper Oxide Nanoparticles, *Acta Sci. Nat.*, 2019, **6**(1), 63–72, DOI: 10.2478/asn-2019-0009.

18 R. M. Adnan, M. Mezher, A. M. Abdallah, R. Awad and M. I. Khalil, Synthesis, Characterization, and Antibacterial Activity of Mg-Doped CuO Nanoparticles, *Molecules*, 2023, **28**(1), 103, DOI: 10.3390/molecules28010103.

19 T. Theivasanthi and M. Alagar, Studies of Copper Nanoparticles Effects on Micro-organisms, *arXiv*, 2011, preprint, arXiv:1110.1372, DOI: 10.48550/arXiv.1110.1372.

20 N. El-Kattan, *et al.*, Evaluation of the antimicrobial activity of chitosan- and curcumin-capped copper oxide nanostructures against multi-drug-resistant microorganisms, *Nanoscale Adv.*, 2025, **7**(10), 2988–3007, DOI: 10.1039/d4na00955j.

21 D. V. Francis, M. N. Jayakumar, H. Ahmad and T. Gokhale, Antimicrobial Activity of Biogenic Metal Oxide Nanoparticles and Their Synergistic Effect on Clinical Pathogens, *Int. J. Mol. Sci.*, 2023, **24**(12), 9998, DOI: 10.3390/ijms24129998.

22 F. Neese, *ORCA Input Library - DFT calculations*, 2021, https://sites.google.com/site/orcainputlibrary/dft-calculations?pli=1.

23 S. Yuan, H. C. S. Chan and Z. Hu, Using PyMOL as a platform for computational drug design, *Wiley Interdiscip. Rev.: Comput. Mol. Sci.*, 2017, **7**(2), e1298, DOI: 10.1002/wcms.1298.

24 L. T. Kaplan W, Software review Swiss-PDB Viewer (Deep View), *Briefings Bioinf.*, 2001, **2**(2), 195–197.

25 P. R. U. Sing, A. C. C. Arbon and F. I. Acf, R Eductions in Cod and a Cute Toxicity of, *Nucleic Acids Res.*, 2012, **9999**(1), 1–8.

26 P. Banerjee, A. O. Eckert, A. K. Schrey and R. Preissner, ProTox-II: A webserver for the prediction of toxicity of chemicals, *Nucleic Acids Res.*, 2018, **46**(W1), W257–W263, DOI: 10.1093/nar/gky318.

27 M. N. Drwal, P. Banerjee, M. Dunkel, M. R. Wettig and R. Preissner, ProTox: A web server for the in silico prediction of rodent oral toxicity, *Nucleic Acids Res.*, 2014, **42**(W1), 53–58, DOI: 10.1093/nar/gku401.

28 J. Eppakayala, P. Donta, J. R. Madireddy, L. Eppakayala, M. R. Mettu and R. Golconda, Synthesis, structural and

optical properties of Ni doped CuO nanoparticles, *Mater. Today: Proc.*, 2023, **92**(April), 679–682, DOI: **10.1016/j.matpr.2023.04.177**.

29 J. Jassi, V. Biju and A. Shajan, Structural and optical properties of zinc oxide nanoparticles, *AIP Conf. Proc.*, 2020, **2263**, 060006, DOI: **10.1063/5.0017263**.

30 N. Khlifi, *et al.*, Non-doped and transition metal-doped CuO nano-powders: structure-physical properties and anti-adhesion activity relationship, *RSC Adv.*, 2022, **12**(36), 23527–23543, DOI: **10.1039/d2ra02433k**.

31 M. A. Ansari and N. Jahan, A Novel Co-Precipitation Route for the Synthesis of Pure and Ni-Doped CuO Nanoparticles: Effect of Doping on Structural, Optical, and Electrical Properties, *Int. J. Nanosci. Nanotechnol.*, 2023, **19**(2), 65–76, DOI: **10.22034/ijnn.2023.555186.2219**.

32 D. Litra, M. Chiriac, N. Ababii and O. Lupan, Acetone Sensors Based on Al-Coated and Ni-Doped Copper Oxide Nanocrystalline Thin Films, *Sensors*, 2024, **24**(20), 6550, DOI: **10.3390/s24206550**.

33 A. Pramothkumar, N. Senthilkumar, K. C. Mercy Gnana Malar, M. Meena and I. Vetha Potheher, A comparative analysis on the dye degradation efficiency of pure, Co, Ni and Mn-doped CuO nanoparticles, *J. Mater. Sci.: Mater. Electron.*, 2019, **30**(20), 19043–19059, DOI: **10.1007/s10854-019-02262-4**.

34 Y. S. Jara, E. T. Mohammed and T. T. Mekiso, Biosynthesized pure CuO, N-CuO, Zn-CuO, and N-Zn-CuO nanoparticles for photocatalytic activity: Enhanced optical properties through bandgap engineering, *Next Mater.*, 2025, **8**, 100742, DOI: **10.1016/j.nxmate.2025.100742**.

35 M. C. Roopa, S. Kallimani, K. Harish Kumar and S. Thirumala, Green-Fueled synthesis of rGO/CuO for catalytic degradation of methyl violet dye, *Chem. Inorg. Mater.*, 2024, **4**, 100077, DOI: **10.1016/j.cinorg.2024.100077**.

36 M. Mousavi-Kamazani, R. Rahmatolahzadeh and F. Beshkar, Facile Solvothermal Synthesis of CeO_2–CuO Nanocomposite Photocatalyst Using Novel Precursors with Enhanced Photocatalytic Performance in Dye Degradation, *J. Inorg. Organomet. Polym. Mater.*, 2017, **27**(5), 1342–1350, DOI: **10.1007/s10904-017-0588-7**.

37 H. Fatimah, *et al.*, Removal of methyl violet dye by a photocatalytic process using variations of TiO_2/zeolite synthesized from muscovite raw material, *J. Ecol. Eng.*, 2025, **26**(5), 73–86, DOI: **10.12911/22998993/200503**.

38 S. Zhang, Y. Yan, W. Hu and Y. Fan, Mesoporous CuO Prepared in a Natural Deep Eutectic Solvent Medium for Effective Photodegradation of Rhodamine B, *Molecules*, 2023, **28**(14), 5554, DOI: **10.3390/molecules28145554**.

39 M. I. Said, A. A. Othman and E. M. Abd elhakeem, Structural, optical and photocatalytic properties of mesoporous CuO nanoparticles with tunable size and different morphologies, *RSC Adv.*, 2021, **11**, 37801–37813, DOI: **10.1039/D1RA04780A**.

40 L. L. Perreault, F. Colò, G. Meligrana, K. Kim, S. Fiorilli, F. Bella, J. R. Nair, C. Vitale-Brovarone, J. Florek, *et al.*, Spray-Dried Mesoporous Mixed Cu-Ni Oxide@Graphene Nanocomposite Microspheres for High Power and Durable Li-Ion Battery Anodes, *Adv. Energy Mater.*, 2018, **9**(3), 1802438, DOI: **10.1002/aenm.201802438**.

41 S. V. Gudkov, D. E. Burmistrov, P. A. Fomina, S. Z. Validov and V. A. Kozlov, Antibacterial Properties of Copper Oxide Nanoparticles (Review), *Int. J. Mol. Sci.*, 2024, **25**(21), 11563, DOI: **10.3390/ijms252111563**.

42 A. Ślosarczyk, *et al.*, Antimicrobial action and chemical and physical properties of CuO-doped engineered cementitious composites, *Sci. Rep.*, 2023, **13**(1), 1–16, DOI: **10.1038/s41598-023-37673-1**.

43 M. R. Islam, N. Farzana, M. R. Akhond, M. Rahaman, M. J. Islam and I. M. Syed, DFT-aided experimental investigation on the electrochemical performance of hetero-interface-functionalized CuO nanoparticle-decorated MoS_2 nanoflowers for energy storage applications, *Mater. Adv.*, 2024, **5**(6), 2491–2509, DOI: **10.1039/d3ma00858d**.

44 A. Latif, A. Latif, M. Mohsin and I. Ahmad, Density functional theory for nanomaterials : structural and spectroscopic applications — a review, *J. Mol. Model.*, 2025, **31**, 211.

45 K. Ungeheuer, K. W. Marszalek, W. Tokarz, M. Perzanowski, Z. Kąkol and M. Marszalek, DFT electronic structure investigation of chromium ion-implanted cupric oxide thin films dedicated for photovoltaic absorber layers, *Sci. Rep.*, 2024, **14**(1), 1–9, DOI: **10.1038/s41598-024-70442-2**.

46 M. R. Das and P. Mitra, Influence of nickel incorporation on structural, optical and electrical characteristics of SILAR synthesized CuO thin films, *J. Sol-Gel Sci. Technol.*, 2018, **88**, 545–554, DOI: **10.1007/s10971-018-4711-1**.

47 A. Pramothkumar, N. Senthilkumar, K. C. Mercy Gnana Malar, M. Meena and I. V. Potheher, A comparative analysis on the dye degradation efficiency of pure, Co, Ni and Mn-doped CuO nanoparticles, *J. Mater. Sci.: Mater. Electron.*, 2019, **30**, 17103–17114, DOI: **10.1007/s10854-019-02262-4**.

48 H. He, Z. Luo and C. Yu, Multifunctional $ZnWO_4$ nanoparticles for photocatalytic removal of pollutants and disinfection of bacteria, *J. Photochem. Photobiol., A*, 2020, **401**, 112735.

49 H. He, Z. Luo and C. Yu, Embellish zinc tungstate nanorods with silver chloride nanoparticles for enhanced photocatalytic, antibacterial and antifouling performance, *Colloids Surf., A*, 2021, **613**, 126099, DOI: **10.1016/j.colsurfa.2020.126099**.

50 Dassault Systèmes BIOVIA, *BIOVIA Discovery Studio Visualizer*, 3DEXPERIENCE Co., 2016, pp. 1–2, **http://accelrys.com**.

51 A. F. M. Sanaullah, R. Hossen, S. Rahman and H. Babu, Synthesis, antimicrobial evaluation , docking and dynamics investigation of novel stearoyl mannopyranosides Synthesis , antimicrobial evaluation , docking and dynamics investigation of novel stearoyl mannopyranosides, *Chem. Phys. Impact*, 2024, **10**, 100799, DOI: **10.1016/j.chphi.2024.100799**.

52 G. Xiong, *et al.*, ADMETlab 2.0: An integrated online platform for accurate and comprehensive predictions of

ADMET properties, *Nucleic Acids Res.*, 2021, **49**(W1), W5–W14, DOI: **10.1093/nar/gkab255**.

53 I. Gosens, *et al.*, Comparative hazard identification by a single dose lung exposure of zinc oxide and silver nanomaterials in mice, *PLoS One*, 2015, **10**(5), 1–17, DOI: **10.1371/journal.pone.0126934**.

54 I. M. Taremwa, I. Ndeze, B. Mwambi, C. Atuhairwe, D. I. Achieng and B. Natukunda, Corrigendum: Assessment of the diagnostic performance of truehb® point-of-care hemometer compared with sysmex i3 analyzer among patients at international hospital Kampala, Uganda (J Blood Med. (2019)10, (85-92)), *J. Blood Med.*, 2019, **10**, 145, DOI: **10.2147/JBM.S217877**.

55 R. Huang, *et al.*, Tox21 challenge to build predictive models of nuclear receptor and stress response pathways as mediated by exposure to environmental chemicals and drugs, *Front. Environ. Sci.*, 2016, **3**, 1–9, DOI: **10.3389/fenvs.2015.00085**.

56 S. Di Bucchianico, *et al.*, Calcium-dependent cyto- and genotoxicity of nickel metal and nickel oxide nanoparticles in human lung cells, *Part. Fibre Toxicol.*, 2018, **15**(1), 1–14, DOI: **10.1186/s12989-018-0268-y**.

57 M. A. Abdulsattar and M. T. Matrood, Spin Multiplicity Effects on Electronic and Spectroscopic Properties of NiO Diatomic Molecule: A DFT Study, *AIP Conf. Proc.*, 2023, **2845**(1), 070029, DOI: **10.1063/5.0157089**.

58 O. Castro-Ocampo, *et al.*, Exploring the CO_2 photocatalytic evolution onto the CuO (1 1 0) surface: A combined theoretical and experimental study, *Heliyon*, 2023, **9**(10), e20134, DOI: **10.1016/j.heliyon.2023.e20134**.

59 N. C. D. Reddy, P. Ramakrishna Reddy and P. S. Reddy, Developing efficient CuO nanoplate/ZnO nanoparticle hybrid photocatalysts for methylene blue degradation under visible light, *RSC Adv.*, 2023, **13**(37), 25849–25860, DOI: **10.1039/D3RA03791F**.

60 Q. Lan, S. Sun, P. Wu, Q. Yang and Y. Liu, Co-doped CuO/Visible Light Synergistic Activation of PMS for Degradation of Rhodamine B and Its Mechanism, *J. Inorg. Mater.*, 2021, **36**(11), 1171–1177, DOI: **10.15541/jim20210090**.

61 A. Khalid, P. Ahmad, A. I. Alharthi, S. Muhammad, M. U. Khandaker, M. Rehman, *et al.*, Structural, Optical, and Antibacterial Efficacy of Pure and Zinc-Doped Copper Oxide Against Pathogenic Bacteria, *Nanomaterials*, 2021, **11**(2), 451, DOI: **10.3390/nano11020451**.